Plasmonic Percolation: Plasmon-Manifested Dielectric-to-Metal Transition

Huanjun Chen,[†] Feng Wang,[†,‡] Kun Li,[§] Kat Choi Woo,[†] Jianfang Wang,[*,†] Quan Li,[†] Ling-Dong Sun,[‡] Xixiang Zhang,[§] Hai-Qing Lin,[†,⊥] and Chun-Hua Yan[‡]

[†]Department of Physics, The Chinese University of Hong Kong, Shatin, Hong Kong SAR, China, [‡]State Key Lab of Rare Earth Materials Chemistry and Applications, Peking University, Beijing 100871, China, [§]Advanced Nanofabrication, Imaging and Characterization Core Lab, King Abdullah University of Science and Technology, Thuwal 23955, Kingdom of Saudi Arabia, and [⊥]Beijing Computational Science Research Center, Beijing 100084, China

ABSTRACT Percolation generally refers to the phenomenon of abrupt variations in electrical, magnetic, or optical properties caused by gradual volume fraction changes of one component across a threshold in bicomponent systems. Percolation behaviors have usually been observed in macroscopic systems, with most studies devoted to electrical percolation.

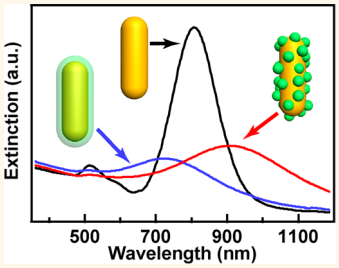

We report on our observation of plasmonic percolation in Au nanorod core—Pd shell nanostructures. When the Pd volume fraction in the shell consisting of palladium and water approaches the plasmonic percolation threshold, ~70%, the plasmon of the nanostructure transits from red to blue shifts with respect to that of the unshelled Au nanorod. This plasmonic percolation behavior is also confirmed by the scattering measurements on the individual core—shell nanostructures. Quasistatic theory and numerical simulations show that the plasmonic percolation originates from a positive-to-negative transition in the real part of the dielectric function of the shell as the Pd volume fraction is increased. The observed plasmonic percolation is found to be independent of the metal type in the shell. Moreover, compared to the unshelled Au nanorods with similar plasmon wavelengths, the Au nanorod core—Pd shell nanostructures exhibit larger refractive index sensitivities, which is ascribed to the expulsion of the electric field intensity from the Au nanorod core by the adsorbed Pd nanoparticles.

KEYWORDS: core—shell nanostructures · gold nanorods · localized surface plasmon resonance · percolation · plasmon shifts · refractive index sensitivity

Percolation is a universal phenomenon in physics, chemistry, and materials science. It is usually related to the dependence of physical properties, such as electrical conductivity, electric and magnetic susceptibility, optical reflectance, and transmittance, on the volume fraction of one component in bicomponent systems.[1−6] If the volume fraction of the component is increased above a value of p_c, a particular physical property of the system will undergo an abrupt change.[7] The value p_c, which is dependent on the dimensionality of the system, is called the percolation threshold. Such a transition is associated with the formation of continuously connecting paths among the different domains of the components in the system. The transition can be discontinuous or continuous, which correspond to first- or second-order transitions, respectively.

The percolation phenomenon, being one of the most challenging problems in the field of inhomogeneous materials, has been constantly attracting scientists. Due to their disordered nature, inhomogeneous materials can differ greatly in their electrical and optical properties from their related single-component counterparts. Electrical percolation has been one of the most intensively studied properties of inhomogeneous systems. The motivation is largely driven by its importance in both fundamental physics and electronic applications.[1−3,5,6] For example, the electrical conductivity of a metal—insulator composite was found to obey a scaling behavior as the volume fraction of the metal component approaches the percolation threshold.[8−12] Such a scaling behavior opens up the opportunity for the fabrication of electronic devices with low-cost, highly electrically conductive metal—insulator composites. Recent studies showed that by dispersing carbon nanotubes into polymers, the electrical transport properties of the composites can be tailored by utilizing electrical percolation.[2−4,6] Very sharp rises in the conductivity of the composites can often be obtained as the nanotube volume fraction is increased across the percolation threshold.[5,13] Moreover, the percolation threshold can be substantially lowered by using carbon nanotubes with large aspect ratios or by mixing carbon

* Address correspondence to jfwang@phy.cuhk.edu.hk.

Received for review May 20, 2012 and accepted July 3, 2012.

Published online July 04, 2012
10.1021/nn302220y

nanotubes with colloidal polymer particles of different sizes and shapes.[5,6] These improved electrical properties enable the production of conductive composites without degrading polymer functionalities, making these composites highly useful for the fabrication of stretchable flat-panel displays and photovoltaic devices.[14]

On the other hand, optical percolation, although less studied than electrical percolation, has been observed in randomly distributed metal–dielectric composites, such as semicontinuous thin metal films.[15–17] Semicontinuous metal films are composed of randomly distributed metal islands, which exhibit localized surface plasmon resonances. Above the percolation threshold, the localized plasmon resonances of individual islands are coupled together along various connecting paths. This coherent interaction can lead to many intriguing optical properties, such as giant electric field enhancements,[15,18] remarkable electric field fluctuations,[15,18,19] and anomalous absorption, reflection, and transmission.[20,21] Understanding the percolation behavior in disordered metal–dielectric films can therefore help in developing optical methods for high-performance sensing, computing, and data storage, as well as in building theoretical models for the electromagnetic responses of disordered systems.

Previous studies on disordered metal–dielectric films have focused mainly on the optical properties of macroscopic semicontinuous metal films. Near the percolation threshold, the optical responses of the films are governed by the collective plasmon resonances resulting from the localized plasmon interactions among different metal islands. Such interactions can bring about many intriguing optical properties. For example, as the density of Au or Ag nanoparticles deposited on transparent substrates is gradually increased, the overall plasmon resonance of the ensemble nanoparticles red-shifts, causing the observed color to exhibit vivid changes.[22] In another study, nanoporous gold with a complex three-dimensional network has been found to possess a very low volume fraction of gold at the percolation transition point. Around the percolation threshold, nanoporous Au films exhibit nearly constant absorption or transmission over a wide spectral range.[23] However, to date, whether plasmonic percolation can occur and how it behaves at sizes below the wavelength of light have been rarely explored. We note that these questions have been tackled in a recent study by considering, from a theoretical perspective, the effect of a conductive junction between two Au nanoshells on their plasmonic response. As the conductance in the junction is gradually increased, the bonding plasmon mode blue-shifts and broadens. At large conductance values, a low-energy charge-transfer plasmon mode appears on the spectrum, with its line width decreasing with increasing conductance values.[24] Nevertheless, to ascertain such variation behaviors experimentally has remained difficult. The challenges lie in how to construct metal–dielectric composite systems at the nanoscale and how to measure the optical properties associated with the compositional variation. Free-standing noble metal nanocrystals, which exhibit rich localized plasmon resonances, provide a viable solution. Their plasmon resonances are dependent sensitively on the geometry, material, spatial arrangement, and surrounding environment.[25–27] The responses of localized plasmons to the changes in these parameters can be readily probed in the far field, as demonstrated widely by the applications of localized plasmons in areas ranging from biosensing[28] and surface-enhanced spectroscopies[29] to optoelectronic circuits.[30] In the present work, we use Au nanorod core–Pd shell nanostructures to elucidate plasmonic percolation at the nanoscale. The Pd shell, being composed of either discrete Pd nanoparticles or a continuous Pd layer, and the surrounding medium, water, provide a metal–dielectric environment for studying plasmonic percolation. Au nanorods, with their longitudinal plasmon resonances far away from the interband transition, function as a probe for revealing the percolation behavior.

RESULTS AND DISCUSSION

The Au nanorod core–Pd shell nanostructures with varying Pd volume fractions in the shell layer were prepared through seed-mediated growth.[31,32] The two extreme cases are illustrated in Figure 1, where the nanorod cores are either coated with a continuous Pd shell or covered with discrete Pd nanoparticles (Figure 1a). The unshelled Au nanorod cores, which have an average length/diameter of $(44 \pm 5)/(12 \pm 1)$ nm, exhibit a longitudinal plasmon resonance at 810 nm when dispersed in water (Figure 1b). After the Au nanorod cores are coated with a continuous Pd shell, as shown by the transmission electron microscopy (TEM) image (Figure 1c), the plasmon resonance is blue-shifted to 730 nm. The coating of a continuous Pd shell is verified by high-angle annular dark-field scanning transmission electron microscopy (HAADF-STEM) imaging and elemental mapping (Figure 1d), from which the thickness of the continuous Pd shell is measured to be 4 ± 2 nm.

The blue shift of the plasmon resonance brought about by coating a continuous Pd shell can be understood by considering the real part of the metal dielectric function. For a small metal nanocrystal immersed in a dielectric medium, at its plasmon resonance, the relation between the real part of the metal dielectric function ε'_m and the integrals of the time-averaged electric field intensity $\bar{E}_2$ is described by[33]

$$-\varepsilon'_m = \int_{\Omega_{dielectric}} \varepsilon_d \overline{E^2}\, dV \Big/ \int_{\Omega_{metal}} \overline{E^2}\, dV \qquad (1)$$

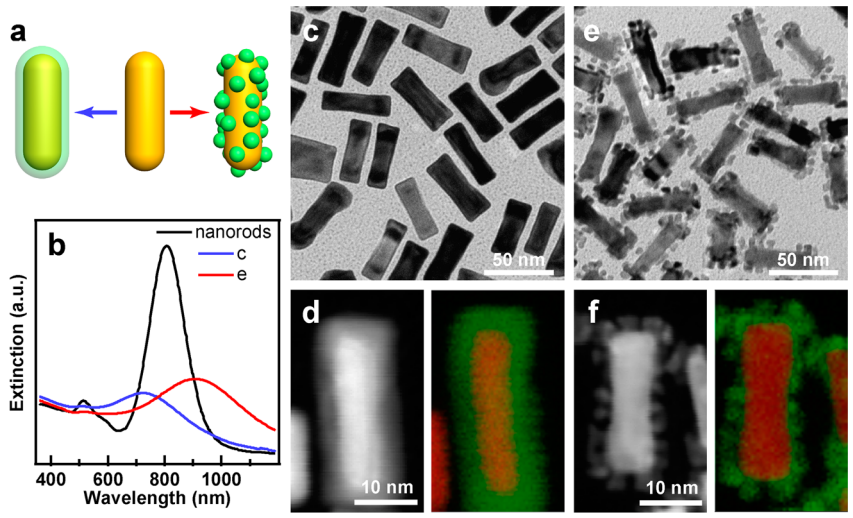

Figure 1. Au nanorod cores coated with a continuous Pd shell or covered with discrete Pd nanoparticles. (a) Schematic of the nanostructures. (b) Extinction spectra of the unshelled Au nanorods (black), the nanostructure sample with a continuous Pd shell (blue), and the one with discrete Pd nanoparticles (red). (c) TEM image of the nanostructures with a continuous Pd shell. (d) HAADF-STEM image (left) and merged elemental map (right) of a single nanostructure with a continuous Pd shell. The nanostructures in (c) and (d) are from the same sample. Its extinction spectrum is shown in (b) as the blue curve. (e) TEM image of the nanostructures with discrete Pd nanoparticles. (f) HAADF-STEM image (left) and merged elemental map (right) of a single nanostructure with discrete Pd nanoparticles. The nanostructures in (e) and (f) are from the same sample. Its extinction spectrum is shown in (b) as the red curve. The red and green colors in the elemental maps stand for gold and palladium, respectively.

where ε_d is the real part of the dielectric constant of the surrounding medium, and Ω_{metal} and $\Omega_{dielectric}$ denote the volumes occupied by the metal and dielectric medium, respectively. If a shell layer is coated on the metal nanocrystal, eq 1 should be rewritten as

$$-\varepsilon'_m = \left(\int_{\Omega'_{dielectric}} \varepsilon_d \overline{E^2}\, dV + \int_{\Omega_{shell}} \varepsilon'_{shell} \overline{E^2}\, dV\right) / \int_{\Omega_{metal}} \overline{E^2}\, dV \quad (2)$$

where ε'_{shell} and Ω_{shell} are the real part of the dielectric function and the volume of the shell layer, respectively, and $\Omega'_{dielectric}$ is the volume of the surrounding medium excluding the shell. The real parts of the dielectric functions of noble metals are typically negative and increase monotonically with decreasing wavelengths (Figure S1, Supporting Information). We can see from eq 2 that a negative ε'_{shell} causes a blue shift in the plasmon resonance of the Au nanorod core, which is in agreement with the experimental observation (Figure 1b).

In comparison, interestingly, when the continuous Pd shell is replaced with a discontinuous one (Figure 1e), the plasmon resonance is red-shifted to 910 nm. As revealed by HAADF-STEM imaging and elemental mapping, the discontinuous Pd shell is composed of many small Pd nanoparticles of 4–5 nm in diameter (Figure 1f). According to eq 2, the discontinuous Pd shell behaves like a dielectric shell. It has a positive ε'_{shell}. These two distinct plasmon shifts suggest that the Pd shell can be either metallic or dielectric, depending on the Pd volume fraction in the shell.

In our experiments, we deliberately utilized Au nanorods with relatively flat ends[34] (Figure S2, Supporting Information) as the cores in order to preclude the plasmon shift caused by the change in the end shape. In addition, the aspect ratios of the unshelled Au nanorods and the core–shell nanostructures with a continuous Pd shell are 3.6 ± 0.5 and 3.2 ± 0.4, respectively. This small difference in their aspect ratios cannot produce a blue shift as large as 80 nm. The blue shift of the plasmon resonance is therefore attributed to the coating of a continuous Pd shell. In order to elucidate more clearly the dependence of the plasmon resonance on the Pd shell, we prepared Au nanorod core–Pd shell nanostructures with increasing Pd volume fractions and measured their extinction spectra (Figure 2). The Pd volume fraction, *p*, in the shell was estimated according to the number of Pd nanoparticles in a projected area and the average size of the Pd nanoparticles. The Au nanorod core was assumed as a cylinder capped with a hemisphere at each end. The plasmon resonance is seen to first red-shift with increasing *p*, reaches a maximum wavelength of 910 nm when *p* is 44%, and then shifts back toward the shorter wavelength region as *p* is further increased. When *p* is equal to 70%, the plasmon resonance is located at 760 nm, which is shorter than the plasmon wavelength of the unshelled Au nanorod cores. The plasmon resonance is finally located at 700 nm when *p* is 100%, which corresponds to a continuous Pd shell. The two core–shell nanostructure samples with a continuous Pd shell, as shown in Figures 1c and 2g, were prepared by heteroepitaxial overgrowth and gradual enlargement of Pd nanoparticles, respectively. The average thickness of the

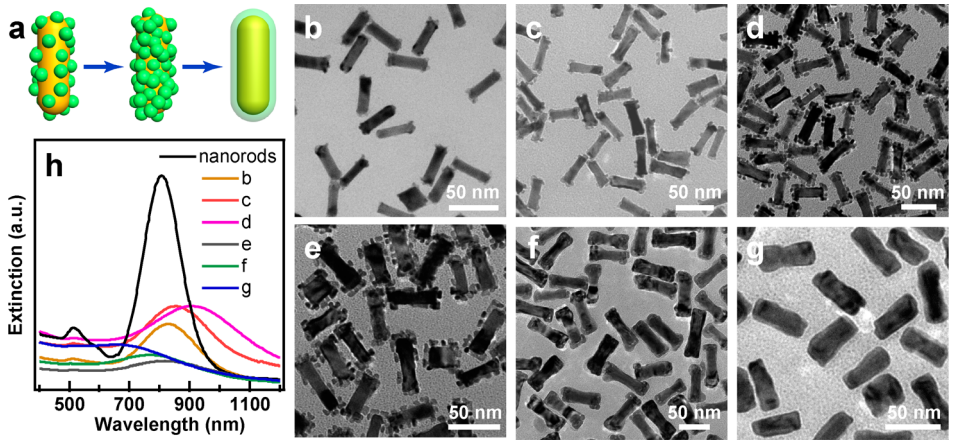

Figure 2. Au nanorod core−Pd shell nanostructures with varying Pd volume fractions. (a) Schematic illustrating the variation of the Pd volume fraction in the shell. (b−g) TEM images of the nanostructure samples with the Pd volume fractions at (7 ± 4)%, (26 ± 5)%, (44 ± 7)%, (56 ± 8)%, (70 ± 5)%, and 100%, respectively. (h) Extinction spectra of the unshelled Au nanorods and the six nanostructure samples shown in (b−g).

continuous Pd shell of the latter sample is measured to be 5 ± 2 nm, which is very close to that of the former one. The close plasmon wavelengths of the two samples corroborate that a continuous Pd shell induces a blue plasmon shift.

The observed variation of the plasmon wavelength with the Pd volume fraction p suggests a plasmonic percolation behavior. There exists a critical Pd volume fraction, p_c, in the shell. Across p_c, the plasmon resonance changes from red to blue shifts with respect to that of the unshelled Au nanorod core. p_c is therefore the plasmonic percolation threshold. It is found experimentally to be ~70%. Unlike in macroscopic disordered metal films, where the changes of physical properties, such as conductivity,[5] across the percolation threshold are abrupt, the plasmonic change in our core−shell nanostructures across p_c is continuous. Therefore, the plasmonic percolation in the core−shell nanostructures belongs to a second-order-like transition, which can be viewed as an intrinsic characteristic of localized plasmons.

A question arises naturally from the above results: what is the underlying mechanism that governs the plasmonic percolation in the Au nanorod core−Pd shell nanostructures? The plasmon wavelengths of metal nanocrystals are sensitively dependent on their surrounding environment.[35] The Pd shell in the nanostructure can be treated as a composite of Pd nanoparticles and water. The increase in the Pd volume fraction leads only to a composition change in the shell, with the Au nanorod core remaining intact. Because the effect of the surrounding environment on the plasmonic properties of metal nanocrystals is essentially determined by its dielectric function, we reason that the plasmonic percolation behavior in the nanostructures is governed by the dielectric variation in the shell. To examine this point, we employed effective-medium approximation (EMA) to calculate the dielectric function of the shell as a function of the Pd volume fraction and thereafter the extinction spectra of the core−shell nanostructures.

In our calculations with the EMA model,[36] the nanostructure was modeled as a prolate spheroid core with the three principal semiaxes of a = 23 nm and $b = c$ = 7 nm. The core was coated with a 5-nm-thick shell. The calculated extinction spectra (Figure 3a) of the nanostructures are consistent with the experimental results (Figure 2h). As p is increased from 0%, the plasmon first red-shifts and reaches a maximum wavelength at p = 34%. With further increases in p, the plasmon shifts back gradually. The transition at which the plasmon resonance changes from red to blue shifts relative to that of the unshelled Au nanorod occurs at p = 66%. When p reaches 100%, the plasmon resonance is located at 650 nm. We also verified the EMA results with numerical finite-difference time-domain (FDTD) simulations by considering only the geometry of the nanostructures and using the dielectric functions of the corresponding bulk materials. The EMA and FDTD (Figure S3, Supporting Information) results show a close resemblance in the overall plasmonic percolation behavior. The p values determined from the EMA modeling for the maximal plasmon wavelength and the percolation threshold are 34% and 66%, and those from the FDTD simulations are 34% and 68%. These values are close to the experimental ones of 44% and 70%, respectively.

The agreements between the EMA and FDTD results prove the validity of the EMA modeling in describing the dielectric function of the composite shell in the nanostructure. We therefore further analyzed the dielectric function of the shell and its effect on the plasmon resonance. The real part ε' is strikingly different from those of water and bulk palladium (Figure 3b). In the visible and near-infrared spectral regions, as p is increased gradually, ε' first increases until p = 20% and

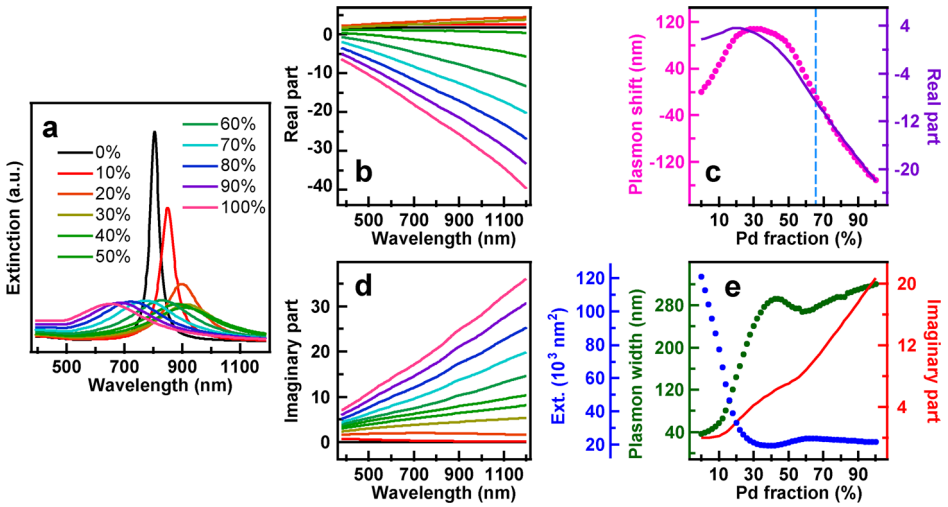

Figure 3. EMA modeling of the plasmonic percolation behavior. (a) Extinction spectra of the Au nanorod core−Pd shell nanostructures. (b) Real parts of the dielectric functions. (c) Dependence of the plasmon shift (pink, left axis) and the real part of the dielectric function at 810 nm (purple, right axis) on the Pd volume fraction. The blue vertical line indicates the percolation threshold. (d) Imaginary parts of the dielectric functions. (e) Dependence of the plasmon peak intensity (blue, left axis), width (green, left axis), and the imaginary part of the dielectric function at 810 nm (red, right axis) on the Pd volume fraction. The different colors for the real parts in (b) and imaginary parts in (d) of the dielectric functions indicate the different Pd volume fractions shown in (a).

then decreases. In particular, when p reaches above 46%, ε' becomes negative, implying that the shell undergoes a transition from being dielectric-like to metal-like. To further unravel the relationship between the plasmon wavelength and the dielectric property of the shell, we extracted ε' at 810 nm, the plasmon wavelength of the unshelled Au nanorod, and plotted it together with the plasmon shift as a function of p (Figure 3c). Clearly, the variation of the plasmon shift follows that of ε'. An interesting observation is that the EMA percolation threshold p_c of 66% does not coincide with the value of 46%, where ε' becomes negative. The threshold value where ε' becomes negative is believed to correspond to the percolative contact between the Pd nanoparticles. The discrepancy can be understood by referring to eq 2. The plasmon shift is affected not only by ε' but also by the electric field distribution around the Au nanorod core. The joint effects of ε' and the local field distribution cause the transition from the red to blue shifts to occur at a p_c of 66%. The same explanation also holds for the discrepancy between the maximal red shift of the plasmon and ε'. These discrepancies are a direct consequence of the localized nature of the plasmons in metal nanostructures. Besides the plasmon peak wavelength, the plasmon peak intensity and width are also observed to vary as a function of p. In general, the plasmon intensity and width are affected by the imaginary part of the dielectric function of the shell through plasmon damping. The imaginary part, ε'', of the dielectric function calculated from the EMA model rises monotonically as p is increased (Figure 3d,e). As a result, with increasing p, the plasmon peak intensity first drops rapidly and then stays nearly constant, and the plasmon width increases first rapidly and then gradually (Figure 3e). The variations in the plasmon intensity and width reflect that more kinetic energy associated with the plasmon resonance is absorbed by the shell as more palladium is incorporated.

In order to rule out the possible ambiguities caused by the inhomogeneous size broadening in the ensemble experiments, we prepared larger Au nanorod−Pd shell nanostructures and conducted single-particle dark-field scattering measurements (Figure S4, Supporting Information). The unshelled Au nanorod sample, which has an average length/diameter of (88 ± 6)/(39 ± 3) nm, exhibits a plasmon resonance at 640 nm in aqueous solutions. The ensemble extinction measurements show that the plasmon shifts to 690 nm when p is 46% and to 590 nm when p equals 100%, suggesting the occurrence of plasmon percolation behavior in these larger nanostructures. The scattering spectra recorded from the individual nanostructures show that an unshelled Au nanorod has a plasmon wavelength of 650 nm when it is supported on an indium tin oxide substrate (Figure 4a). When the Au nanorod is decorated with Pd nanoparticles with a p of 46%, the plasmon red-shifts to 700 nm (Figure 4b). When the Au nanorod is coated with a continuous Pd shell, the plasmon blue-shifts to 590 nm (Figure 4c). The single-particle scattering spectra of the different nanostructures can also be reproduced by the EMA modeling and FDTD simulations. The slight deviations between the measured and calculated scattering spectra are ascribed to the inhomogeneous size and shape distributions of the nanostructures and the effect of the substrate on the plasmon resonance.[37]

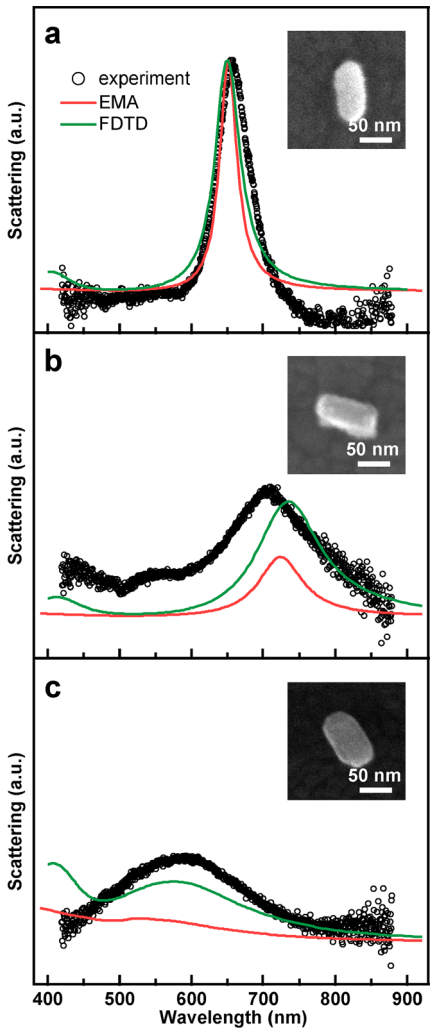

Figure 4. Single-particle scattering spectra of the larger Au nanorod core–Pd shell nanostructures. (a) Unshelled Au nanorod. (b) Nanostructure with a Pd volume fraction of (46 ± 8)%. (c) Nanostructure with a continuous Pd shell. The insets are the scanning electron microscopy images of the corresponding nanostructures. The experimental scattering spectra were acquired on more than 10 nanostructures for each sample. They are similar to one another. For the EMA modeling, the three principal semiaxes of the spheroid core were set at a = 45 nm and b = c = 21 nm. For the FDTD simulations, the diameter and overall length of the Au nanorod core were set at 40 and 91 nm, respectively. The shell thickness was 5 nm for both the modeling and simulations.

The above experiments on the Au nanorod core–Pd shell nanostructures reveal that the plasmonic percolation behavior is determined by the Pd volume fraction. The experimental evidence regarding the plasmonic percolation was also obtained in core–shell nanostructures with Au nanospheres as the cores (Figure S5, Supporting Information) and with the shell composed of silver or platinum (Figure S6, Supporting Information), respectively, although a fine adjustment of the Ag or Pt volume fraction was difficult at this stage. For the Au nanosphere core–Pd shell nanostructures, the unshelled Au nanosphere sample, which has an average diameter of 65 ± 3 nm, exhibits a plasmon wavelength of 534 nm in aqueous solutions. The plasmon red-shifts to 572 nm and blue-shifts to 522 nm when the Pd volume fraction is 50% and 100%, respectively. For the Au nanorod-cored nanostructures with a Ag or a Pt shell, the unshelled Au nanorod sample also has a longitudinal plasmon wavelength of 810 nm in aqueous solutions. The Pt shell on the nanorod core is composed of Pt nanoparticles having an average size of 4 ± 1 nm. Such a discontinuous Pt shell leads to a red shift of 52 nm in the plasmon. In contrast, the Ag shell is continuous, with an average thickness of 3 ± 1 nm. The plasmon of the Au core–Ag shell nanostructures is blue-shifted by 101 nm in comparison to that of the unshelled Au nanorods. These findings suggest that the observed plasmonic percolation is a general phenomenon. It is independent of the metal type in the shell. On the other hand, the percolation threshold p_c is expected to be dependent on the specific geometry as well as the environment of the system. A recent study of electrical percolation showed that the system size and external perturbation, such as electric field or ultraviolet radiation, can have remarkable effects on the metal–insulator transition of random metal–dielectric films.[38] Future work will be needed along this direction to elucidate the effects of these factors on the plasmonic percolation behavior.

We finally studied the refractive index sensitivities of the Au nanorod core–Pd shell nanostructures to explore their potential in sensing applications. The core–shell nanostructures with different Pd volume fractions were respectively dispersed into water–glycerol mixtures of varying volume ratios for the measurements of their extinction spectra.[39] The plasmon shift was plotted *versus* the refractive index of the liquid mixture. The refractive index sensitivity was then determined by linear fitting. The index sensitivity of each core–shell nanostructure sample was then compared to that of the unshelled Au nanorod sample with a similar longitudinal plasmon wavelength when both were dispersed in water, since the index sensitivities of noble metal nanocrystals generally increase with increasing plasmon wavelength.[39] Figure 5a shows as an example the variations of the plasmon shift *versus* the refractive index for a core–shell nanostructure sample and an unshelled nanorod sample. Their longitudinal plasmon wavelengths are 776 and 770 nm, respectively. The Pd volume fraction of the core–shell nanostructure sample is 70%. The index sensitivity, 520 nm per refractive index unit (RIU), of the nanostructure sample is about twice that of the unshelled nanorod sample at 278 nm/RIU, suggesting that the discontinuous Pd shell can enhance the index sensitivity. We also calculated the index sensitivity of these two nanostructure samples using the FDTD method (Figure 5a). The calculated results show that the index sensitivity, 574 nm/RIU, of the core–shell

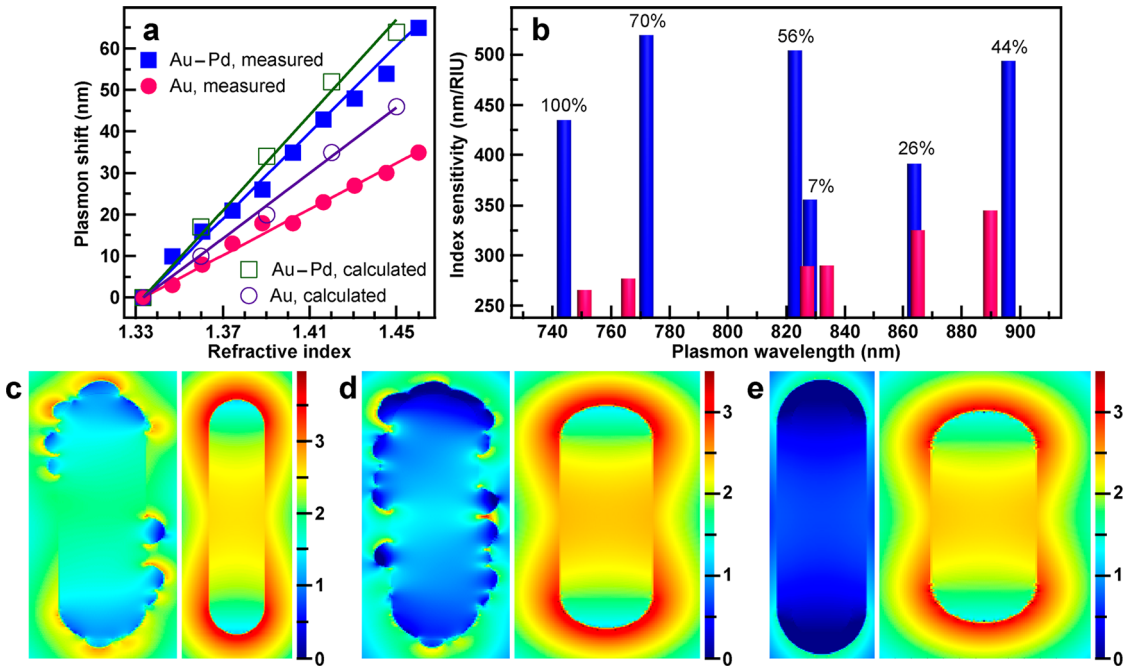

Figure 5. Refractive index sensitivities of the Au nanorod core–Pd shell nanostructures and unshelled Au nanorods. (a) Dependence of the longitudinal plasmon shift on the index for one core–shell nanostructure sample (squares) and one Au nanorod sample (circles), respectively. Both the measured (solid circles and squares) and calculated (hollow circles and squares) points are shown. The lines are linear fits. The Pd volume fraction of the nanostructure sample is 70%. (b) Comparison of the index sensitivities of the core–shell nanostructure samples and the unshelled Au nanorod samples with close longitudinal plasmon wavelengths. The percentages are the Pd volume fractions. The nanostructure samples were prepared following the same procedures as those shown in Figure 2b–g. There are small fluctuations in the plasmon wavelengths. (c–e) Comparison of the electric field intensity enhancement contours of the core–shell nanostructures (left) and the unshelled Au nanorods (right) at the logarithmic scale. For each pair, the plasmon wavelength of the unshelled Au nanorod is adjusted to be equal to that of the core–shell nanostructure by varying the length while keeping the diameter unchanged. The core of the nanostructure has a size of 13 nm by 52 nm. The Pd volume fractions of the nanostructures are 34%, 68%, and 100%, and the diameters/lengths of the Au nanorods are 13/56, 13/46, and 13/37 nm in (c–e), respectively. All of the contours pass through the length axis.

nanostructure sample is much higher than that of the unshelled nanorod sample at 392 nm/RIU. This is qualitatively consistent with the experiment. The discrepancy between the measured and calculated index sensitivity values can be ascribed to the presence of the stabilizing molecules on the surface of the metal nanostructures. The superior index sensitivities of the Au nanorod core–Pd shell nanostructures were further verified by the measurements of the core–shell nanostructure samples with varying Pd volume fractions. In comparison with the unshelled Au nanorod samples, all of the core–shell nanostructure samples exhibit higher index sensitivities (Figure 5b). In addition, except the one with a continuous Pd shell, the index sensitivities of the nanostructure samples generally increase with increasing Pd volume fractions.

The index sensitivity of a metal nanocrystal is determined by how easily the electron oscillation in the nanocrystal can be displaced. The displacement of the electron oscillation is governed by the Coulombic restoring force in the nanocrystal and the electromagnetic screening induced by the surrounding dielectric medium. These two factors depend on the electric field distribution in and around the nanocrystal. Therefore, the underlying mechanism for the index sensitivity enhancement of the core–shell nanostructures can be ascertained by comparing their electric field distributions to those of the corresponding unshelled Au nanorods. Figure 5c shows as an example the field intensity enhancement contours for the case of the nanostructure with a Pd volume fraction of 34%. The field intensity enhancement contour of the unshelled nanorod exhibits a clear dipolar pattern, where the largest enhancement is located at the two ends. In addition, the field intensity inside the nanorod is comparable to that in the surrounding medium, suggesting the presence of a large Coulombic restoring force in the nanorod. In contrast, the field distribution in the nanostructure shows a smeared dipolar nature. The field intensity inside the nanostructure is greatly weakened in the presence of discrete Pd nanoparticles. The expulsion of the electric field out of the nanostructure leads to a reduction in the restoring force. As a result, the displacement of the electron cloud in the nanostructure becomes easier when the refractive index of the surrounding medium is increased, giving rise to an enhanced index sensitivity. The expulsion of the electric field out of the nanostructure is greater

when more Pd nanoparticles are present (Figure 5d). Therefore, the index sensitivity of the nanostructure increases as the Pd volume fraction gets higher. The nanostructure with a continuous Pd shell is an exception, which might be due to its short plasmon wavelength. However, its index sensitivity is still much larger than that of the corresponding unshelled nanorod. More work will be needed for quantitatively understanding the difference in the index sensitivities of the core–shell nanostructures and unshelled Au nanorods. In addition, the figure of merit, which is the ratio between the index sensitivity and plasmon peak width, is often used together with the index sensitivity for characterizing the sensing capabilities of metal nanocrystals. Because the plasmon resonance of the core–shell nanostructure is more broadened as the Pd volume fraction is increased, the figure of merit generally becomes smaller.

CONCLUSION

We have observed the plasmonic percolation behavior on Au nanorod core–Pd shell nanostructures. The plasmon wavelength of the nanostructure is found to be strongly dependent on the Pd volume fraction in the shell. When the Pd volume fraction approaches the plasmonic percolation threshold, ~70%, the plasmon of the nanostructure transits from red to blue shifts with respect to that of the unshelled Au nanorod. Such a plasmonic percolation behavior is ascribed to the positive-to-negative transition in the real part of the dielectric function of the shell as the Pd volume fraction is increased. The plasmonic percolation is further corroborated by both single-particle scattering measurements and numerical FDTD simulations. The observed plasmonic percolation is independent of the metal type in the shell. Moreover, the Au nanorod core–Pd shell nanostructures exhibit enhanced refractive index sensitivities in comparison to unshelled Au nanorods with similar plasmon wavelengths. Our results will be helpful in not only understanding the localized plasmon resonances of multimetallic nanostructures but also designing complex metal nanostructures with desired plasmon-based functionalities.

METHODS

Sample Preparations. All of the core–shell nanostructure samples were prepared in aqueous solutions using seed-mediated growth. The Au nanorod samples, obtained from NanoSeedz, were precipitated by centrifugation and redispersed in water at the same volume. The peak extinction values of the nanorod samples with longitudinal plasmon wavelengths of 810 and 640 nm were 3.3 and 1.3, respectively, in 1 cm cuvettes. For the preparation of the Au nanorod core–Pd shell nanostructure samples with the Au nanorod core having a longitudinal plasmon wavelength of 810 nm, the washed Au nanorod solution (1 mL) was added in a growth solution composed of cetyltrimethylammonium chloride (CTAC, 3 mL, 0.025 M), ascorbic acid (*V*, 0.1 M), and H_2PdCl_4 (2*V*, 0.01 M). *V* was used to denote the volume of the related solution. The obtained solution was mixed by repeated gentle inversion for 10 s and left undisturbed overnight at room temperature. The growths of the nanostructure samples with Pd volume fractions of 7%, 26%, 44%, and 56% were performed with *V* being 2.5, 5, 10, and 15 μL, respectively. The core–shell nanostructure sample with the Pd volume fraction at 70% was produced by subjecting the nanostructure sample with the Pd volume fraction at 56% to another run of the Pd shell growth in a cetyltrimethylammonium bromide (CTAB) solution. Specifically, the solution of the as-grown nanostructure sample with the Pd volume fraction at 56% was centrifuged. The precipitate was redispersed into water at the same volume. The washed nanostructure solution (1 mL) was then added into a growth solution composed of CTAB (3 mL, 0.033 M), ascorbic acid (5 μL, 0.1 M), and H_2PdCl_4 (10 μL, 0.01 M).

Two methods were employed for the preparation of the nanostructure sample with the Pd volume fraction at 100%. The first method was similar to that utilized above for the preparation of the nanostructure sample with the Pd volume fraction at 70%. The volumes of the ascorbic acid and H_2PdCl_4 solutions were changed to 10 and 20 μL, respectively. The second method was to grow a continuous Pd shell directly in a CTAB solution, where the volume of the Au nanorod solution was 1 mL, and the growth solution was composed of CTAB (3 mL, 0.033 M), ascorbic acid (15 μL, 0.1 M), and H_2PdCl_4 (30 μL, 0.01 M).

The Au nanorod core–Pd shell nanostructure samples with the Au nanorod core having a longitudinal plasmon wavelength at 640 nm were prepared by adding the washed Au nanorod solution (1 mL) into a growth solution composed of CTAC (3 mL, 0.025 M), ascorbic acid (10 μL, 0.1 M), and H_2PdCl_4 (20 μL, 0.01 M). The obtained solution was mixed by gentle inversion for 10 s and then left undisturbed overnight at room temperature. The product was centrifuged. The precipitate was redispersed into water (1 mL). The same procedure was utilized for the growth of the nanostructure sample with the Pd volume fraction at 100%, except that the CTAC solution was changed to a CTAB solution (3 mL, 0.033 M).

The Au nanorod core–Ag shell nanostructure sample was prepared by adding the washed Au nanorod sample (2 mL) with a longitudinal plasmon wavelength at 810 nm in a CTAC solution (2 mL, 0.08 M). $AgNO_3$ (0.12 mL, 0.01 M) and ascorbic acid (0.06 mL, 0.1 M) were then supplied. The reaction mixture was heated in an oven at 65 °C for 3 h.

The Au nanorod core–Pt shell nanostructure sample was made by adding the washed Au nanorod sample (1 mL) having a longitudinal plasmon wavelength of 810 nm into a growth solution composed of CTAB (3 mL, 0.033 M), ascorbic acid (0.12 mL, 0.1 M), and H_2PtCl_4 (0.06 mL, 0.01 M). The obtained solution was mixed by gentle inversion for 10 s and then kept in the oven at 65 °C for 6 h.

Characterizations. Low-magnification TEM imaging was carried out on an FEI CM120 microscope. HAADF-STEM imaging and energy-dispersive X-ray elemental mapping were performed on an FEI Tecnai F20 microscope equipped with an Oxford energy-dispersive X-ray analysis system. Scanning electron microscopy images were acquired on an FEI Quanta 400 FEG microscope. Extinction spectra were measured on a Hitachi U-3501 UV/visible/NIR spectrophotometer. Single-particle scattering measurements were performed on a dark-field optical microscope (Olympus BX60) that was integrated with a quartz–tungsten–halogen lamp (100 W), a monochromator (Acton SpectraPro 2300i), and a charge-coupled device camera (Princeton Instruments Pixis 512B). During the measurements, the camera was thermoelectrically cooled to −70 °C. A dark-field objective (100×, numerical aperture: 0.80) was employed for both illuminating the nanostructures with the white light and collecting the scattered light. The scattering spectrum from

an individual nanostructure was corrected by first subtracting the background spectrum taken from the adjacent region without metal nanostructures and then dividing it with the calibrated response curve of the entire optical system.

Refractive Index Sensitivity Measurements. Water–glycerol mixtures of varying volume ratios were used to change the refractive index of the surrounding medium of the nanostructures. The volume percentage of glycerol in the liquid mixture was varied from 0% to 90% at steps of 10%. The as-prepared nanostructures were first centrifuged at 12000*g* for 6 min and then redispersed in the liquid mixtures. The extinction spectra of the resultant dispersion solutions of the Au nanostructures were measured. The plasmon shift was plotted as a function of the refractive index. The index sensitivity was determined by linear fitting.

Modeling and Simulations. The EMA model was utilized to calculate the effective dielectric functions of the shell layers with varying Pd volume fractions.[40] In the model, the dielectric function is the solution of the self-consistent relation

$$p\frac{\varepsilon_m - \varepsilon_e}{\varepsilon_m + (\xi - 1)\varepsilon_e} + (1 - p)\frac{\varepsilon_d - \varepsilon_e}{\varepsilon_d + (\xi - 1)\varepsilon_e} = 0 \quad (3)$$

where ε_m, ε_d, and ε_e are the dielectric functions of the metal, dielectric, and composite system, respectively. In the core–shell nanostructures, ε_m and ε_d are the dielectric functions of palladium and water, respectively. The volume fraction of palladium in the shell is denoted by p. The parameter ξ is determined by the dimensionality of the system and the geometry of the metal component. In our system, the Pd component is approximated as being composed of spherical nanoparticles. Under this approximation, ξ is equal to 3.

Once the effective dielectric function of the shell layer is determined according to eq 3, the extinction and scattering spectra of the Au nanorod core–Pd shell nanostructures can be simulated on the basis of a core–shell prolate spheroid model under quasistatic approximation. The three principal semiaxes, a, b, and c, of the core spheroid were determined from the TEM images of the nanostructure sample. For the Au nanorods with a longitudinal plasmon wavelength of 810 nm, the values are a = 23 nm and $b = c = 7$ nm. For the Au nanorods with a longitudinal plasmon wavelength of 640 nm, the values are a = 45 nm and $b = c$ = 21 nm. The thickness d of the Pd shell was set at 5 nm. In our calculations, we considered only the excitation along the length axis of the nanostructure. The electric polarizability of the core–shell nanostructure along the length axis is given by eq 4,[41]

$$\alpha_a = \frac{V\{(\varepsilon_e - \varepsilon_d)[\varepsilon_e + (\varepsilon_{Au} - \varepsilon_e)(L_a^{(1)} - fL_a^{(2)})] + f\varepsilon_e(\varepsilon_{Au} - \varepsilon_e)\}}{[\varepsilon_e + (\varepsilon_{Au} - \varepsilon_e)(L_a^{(1)} - fL_a^{(2)})][\varepsilon_d + (\varepsilon_e - \varepsilon_d)L_a^{(2)}] + fL_a^{(2)}\varepsilon_e(\varepsilon_{Au} - \varepsilon_e)} \quad (4)$$

where V is the volume of the entire core–shell nanostructure, ε_{Au} is the dielectric function of gold, f is the fraction of the total particle volume occupied by the inner spheroid, and $L_a^{(1)}$ and $L_a^{(2)}$ are the geometrical factors for the inner and outer spheroids.

$$L_a^{(j)} = \frac{a_j b_j c_j}{2}\int_0^\infty \frac{dq}{(a_j^2 + q)f_j(q)} \quad j = 1, 2 \quad (5)$$

In eq 5, a_j, b_j, and c_j are the three principal semiaxes of the core (j = 1) and shell (j = 2), respectively. $f_j(q)$ is given by

$$f_j(q) = [(a_j^2 + q)(b_j^2 + q)(c_j^2 + q)]^{1/2} \quad (6)$$

The scattering, absorption, and extinction cross sections of the nanostructure can thereafter be obtained from

$$C_{sca} = \frac{k^4}{6\pi}|\alpha_a|^2 \quad (7)$$

$$C_{abs} = k\,\mathrm{Im}(\alpha_a) \quad (8)$$

$$C_{ext} = C_{abs} + C_{sca} \quad (9)$$

where $k = (2\pi(\varepsilon_d)^{1/2})/\lambda$ is the wavevector. When the nanostructures are dispersed in water, ε_d is equal to 1.778. When the nanostructures are deposited on indium tin oxide substrates, ε_d is equal to 1.

The FDTD simulations were performed using FDTD Solutions 6.0 from Lumerical Solutions. During the calculations, an electromagnetic pulse in the wavelength range 500–900 nm was launched into a box containing the target nanostructure to simulate a propagating plane wave interacting with the nanostructure. The metal nanostructure and its surrounding space were divided into 0.5 nm meshes. The refractive index of the medium was taken to be 1.3334. The Au nanorod core was modeled as a cylinder capped with a hemisphere at each end. Its sizes were set to be the same as the average ones measured from the TEM images. The discontinuous Pd shell was modeled by attaching hemispherical Pd nanoparticles of 10 nm in diameter onto the Au nanorod, with the flat bottom of each Pd nanoparticle in contact with the Au nanorod surface. The number of Pd nanoparticles was determined according to the Pd volume fraction in the shell layer. The continuous Pd shell was modeled by wrapping the Au nanorod core with a 5-nm-thick Pd layer. In the calculations of the field intensity enhancement contours, the diameter of the unshelled Au nanorod was equal to that of the Au nanorod core in the core–shell nanostructure. The longitudinal plasmon wavelength of the unshelled Au nanorod was adjusted by varying its length to match that of the corresponding core–shell nanostructure. When the nanostructures were dispersed in water, the refractive index of the surrounding medium was set as 1.3334. When the nanostructures were deposited on indium tin oxide substrates, the index was set as 1. The refractive index sensitivities of the nanostructures were also determined through the FDTD simulations by varying the index of the surrounding medium.

Conflict of Interest: The authors declare no competing financial interest.

Acknowledgment. This work was supported by the Research Grants Council of Hong Kong (GRF, ref. no. CUHK403211, Project Code 2130277, and Special Equipment Grant, ref. no. SEG_CUHK06).

Supporting Information Available: The real parts of the dielectric functions of gold, silver, palladium, and platinum, TEM images of the unshelled Au nanorods, Au nanorod core–Pd shell, Au nanorod core–Pt shell, and Au nanorod core–Ag shell nanostructures, extinction spectra of the unshelled Au nanorods and core–shell nanostructures, and FDTD-simulated extinction spectra of the Au nanorod core–Pd shell nanostructures with varying Pd volume fractions. This material is available free of charge *via* the Internet at http://pubs.acs.org.

REFERENCES AND NOTES

1. Isichenko, M. B. Percolation, Statistical Topography, and Transport in Random Media. *Rev. Mod. Phys.* **1992**, *64*, 961–1043.
2. Vigolo, B.; Coulon, C.; Maugey, M.; Zakri, C.; Poulin, P. An Experimental Approach to the Percolation of Sticky Nanotubes. *Science* **2005**, *309*, 920–923.
3. Kyrylyuk, A. V.; van der Schoot, P. Continuum Percolation of Carbon Nanotubes in Polymeric and Colloidal Media. *Proc. Natl. Acad. Sci. U. S. A.* **2008**, *105*, 8221–8226.
4. Topinka, M. A.; Rowell, M. W.; Goldhaber-Gordon, D.; McGehee, M. D.; Hecht, D. S.; Gruner, G. Charge Transport in Interpenetrating Networks of Semiconducting and Metallic Carbon Nanotubes. *Nano Lett.* **2009**, *9*, 1866–1871.
5. Nan, C.-W.; Shen, Y.; Ma, J. Physical Properties of Composites near Percolation. *Annu. Rev. Mater. Res.* **2010**, *40*, 131–151.
6. Kyrylyuk, A. V.; Hermant, M. C.; Schilling, T.; Klumperman, B.; Koning, C. E.; van der Schoot, P. Controlling Electrical Percolation in Multicomponent Carbon Nanotube Dispersions. *Nat. Nanotechnol.* **2011**, *6*, 364–369.
7. Achlioptas, D.; D'Souza, R. M.; Spencer, J. Explosive Percolation in Random Networks. *Science* **2009**, *323*, 1453–1455.

8. Stauffer, D.; Aharony, A. *Introduction to Percolation Theory*; Taylor & Francis: Philadelphia, 1994.
9. Zallen, R. *The Physics of Amorphous Solids*; John Wiley & Sons: New York, 1983.
10. Nan, C. W. Physics of Inhomogeneous Inorganic Materials. *Prog. Mater. Sci.* **1993**, *37*, 1–116.
11. Cohen, M. H.; Jortner, J.; Webman, I. Percolation Conductivity in Granular Metal Films. *Phys. Rev. B* **1978**, *17*, 4555–4557.
12. Toker, D.; Azulay, D.; Shimoni, N.; Balberg, I.; Millo, O. Tunneling and Percolation in Metal-Insulator Composite Materials. *Phys. Rev. B* **2003**, *68*, 041403.
13. Bryning, M. B.; Islam, M. F.; Kikkawa, J. M.; Yodh, A. G. Very Low Conductivity Threshold in Bulk Isotropic Single-Walled Carbon Nanotube-Epoxy Composites. *Adv. Mater.* **2005**, *17*, 1186–1191.
14. Cao, Q.; Rogers, J. A. Ultrathin Films of Single-Walled Carbon Nanotubes for Electronics and Sensors: A Review of Fundamental and Applied Aspects. *Adv. Mater.* **2009**, *21*, 29–53.
15. Shalaev, V. M. *Nonlinear Optics of Random Media: Fractal Composites and Metal–Dielectric Films*; Springer: Berlin, 2000.
16. Stockman, M. I.; Faleev, S. V.; Bergman, D. J. Localization *versus* Delocalization of Surface Plasmons in Nanosystems: Can One State Have Both Characteristics? *Phys. Rev. Lett.* **2001**, *87*, 167401.
17. Seal, K.; Genov, D. A.; Sarychev, A. K.; Noh, H.; Shalaev, V. M.; Ying, Z. C.; Zhang, X.; Cao, H. Coexistence of Localized and Delocalized Surface Plasmon Modes in Percolating Metal Films. *Phys. Rev. Lett.* **2006**, *97*, 206103.
18. Seal, K.; Nelson, M. A.; Ying, Z. C.; Genov, D. A.; Sarychev, A. K.; Shalaev, V. M. Growth, Morphology, and Optical and Electrical Properties of Semicontinuous Metallic Films. *Phys. Rev. B* **2003**, *67*, 035318.
19. Sarychev, A. K.; Shalaev, V. M. Electromagnetic Field Fluctuations and Optical Nonlinearities in Metal-Dielectric Composites. *Phys. Rep.* **2000**, *335*, 275–371.
20. Yagil, Y.; Gadenne, P.; Julien, C.; Deutscher, G. Optical Properties of Thin Semicontinuous Gold Films over a Wavelength Range of 2.5 to 500 μm. *Phys. Rev. B* **1992**, *46*, 2503–2511.
21. Brouers, F.; Clerc, J. P.; Giraud, G.; Laugier, J. M.; Randriamantany, Z. A. Dielectric and Optical Properties Close to the Percolation Threshold. II. *Phys. Rev. B* **1993**, *47*, 666–673.
22. Kealley, C. S.; Cortie, M. B.; Maaroof, A. I.; Xu, X. D. The Versatile Colour Gamut of Coatings of Plasmonic Metal Nanoparticles. *Phys. Chem. Chem. Phys.* **2009**, *11*, 5897–5902.
23. Smith, G. B.; Maaroof, A. I.; Cortie, M. B. Percolation in Nanoporous Gold and the Principle of Universality for Two-Dimensional to Hyperdimensional Networks. *Phys. Rev. B* **2008**, *78*, 165418.
24. Pérez-González, O.; Zabala, N.; Borisov, A. G.; Halas, N. J.; Nordlander, P.; Aizpurua, J. Optical Spectroscopy of Conductive Junctions in Plasmonic Cavities. *Nano Lett.* **2010**, *10*, 3090–3095.
25. Sau, T. K.; Rogach, A. L.; Jäckel, F.; Klar, T. A.; Feldmann, J. Properties and Applications of Colloidal Nonspherical Noble Metal Nanoparticles. *Adv. Mater.* **2010**, *22*, 1805–1825.
26. Cortie, M. B.; McDonagh, A. M. Synthesis and Optical Properties of Hybrid and Alloy Plasmonic Nanoparticles. *Chem. Rev.* **2011**, *111*, 3713–3735.
27. Stockman, M. I. Nanoplasmonics: The Physics behind the Applications. *Phys. Today* **2011**, *64*, 39–44.
28. Anker, J. N.; Hall, W. P.; Lyandres, O.; Shah, N. C.; Zhao, J.; Van Duyne, R. P. Biosensing with Plasmonic Nanosensors. *Nat. Mater.* **2008**, *7*, 442–453.
29. Li, J. F.; Huang, Y. F.; Ding, Y.; Yang, Z. L.; Li, S. B.; Zhou, X. S.; Fan, F. R.; Zhang, W.; Zhou, Z. Y.; Wu, D. Y.; *et al.* Shell-Isolated Nanoparticle-Enhanced Raman Spectroscopy. *Nature* **2010**, *464*, 392–395.
30. Maier, S. A.; Kik, P. G.; Atwater, H. A.; Meltzer, S.; Harel, E.; Koel, B. E.; Requicha, A. A. G. Local Detection of Electromagnetic Energy Transport below the Diffraction Limit in Metal Nanoparticle Plasmon Waveguides. *Nat. Mater.* **2003**, *2*, 229–232.
31. Wang, F.; Sun, L.-D.; Feng, W.; Chen, H. J.; Yeung, M. H.; Wang, J. F.; Yan, C.-H. Heteroepitaxial Growth of Core–Shell and Core–Multishell Nanocrystals Composed of Palladium and Gold. *Small* **2010**, *6*, 2566–2575.
32. Zhang, K.; Xiang, Y. J.; Wu, X. C.; Feng, L. L.; He, W. W.; Liu, J. B.; Zhou, W. Y.; Xie, S. S. Enhanced Optical Responses of Au@Pd Core/Shell Nanobars. *Langmuir* **2009**, *25*, 1162–1168.
33. Wang, F.; Shen, Y. R. General Properties of Local Plasmons in Metal Nanostructures. *Phys. Rev. Lett.* **2006**, *97*, 206806.
34. Prescott, S. W.; Mulvaney, P. Gold Nanorod Extinction Spectra. *J. Appl. Phys.* **2006**, *99*, 123504.
35. Sepúlveda, B.; Angelomé, P. C.; Lechuga, L. M.; Liz-Marzán, L. M. LSPR-Based Nanobiosensors. *Nano Today* **2009**, *4*, 244–251.
36. Bruggeman, D. A. G. Berechnung Verschiedener Physikalischer Konstanten von Heterogenen Substanzen. *Ann. Phys. (Leipzig)* **1935**, *24*, 636–679.
37. Chen, H. J.; Shao, L.; Ming, T.; Woo, K. C.; Man, Y. C.; Wang, J. F.; Lin, H.-Q. Observation of the Fano Resonance in Gold Nanorods Supported on High-Dielectric-Constant Substrates. *ACS Nano* **2011**, *5*, 6754–6763.
38. Chen, A. B. K.; Kim, S. G.; Wang, Y. D.; Tung, W.-S.; Chen, I.-W. A Size-Dependent Nanoscale Metal-Insulator Transition in Random Materials. *Nat. Nanotechnol.* **2011**, *6*, 237–241.
39. Chen, H. J.; Kou, X. S.; Yang, Z.; Ni, W. H.; Wang, J. F. Shape- and Size-Dependent Refractive Index Sensitivity of Gold Nanoparticles. *Langmuir* **2008**, *24*, 5233–5237.
40. Cai, W. S.; Genov, D. A.; Shalaev, V. M. Three-Dimensional Array of Dielectric Spheres with an Isotropic Negative Permeability at Infrared Frequencies. *Phys. Rev. B* **2005**, *72*, 193101.
41. Bohren, C. F.; Huffman, D. R. *Absorption and Scattering of Light by Small Particles*; John Wiley & Sons, Inc.: New York, 1983.